Inverse Problems in Science and Engineering
Publication details, including instructions for authors and subscription information:
http://www.tandfonline.com/loi/gipe20

Novel numerical inversions of two circular-arc radon transforms in Compton scattering tomography

Gaël Rigaud [a], Maï K. Nguyen [a] & Alfred K. Louis [b]
[a] Cergy-Pontoise/CNRS, ETIS-ENSEA/University, 95000 Cergy-Pontoise Cedex, France
[b] Fachbereich Mathematik, Universität des Saarlandes, D-66041 Saarbrücken, Germany
Version of record first published: 16 Feb 2012.

To cite this article: Gaël Rigaud , Maï K. Nguyen & Alfred K. Louis (2012): Novel numerical inversions of two circular-arc radon transforms in Compton scattering tomography, Inverse Problems in Science and Engineering, 20:6, 809-839

To link to this article: http://dx.doi.org/10.1080/17415977.2011.653008

Inverse Problems in Science and Engineering
Vol. 20, No. 6, September 2012, 809–839

Taylor & Francis
Taylor & Francis Group

Novel numerical inversions of two circular-arc radon transforms in Compton scattering tomography

Gaël Rigaud[a], Maï K. Nguyen[a]* and Alfred K. Louis[b]

[a]*Cergy-Pontoise/CNRS, ETIS-ENSEA/University, 95000 Cergy-Pontoise Cedex, France;*
[b]*Fachbereich Mathematik, Universität des Saarlandes, D-66041 Saarbrücken, Germany*

(*Received 23 July 2011; final version received 21 December 2011*)

Compton scattering tomography (CST) is an alternative imaging process which reconstructs, in a two-dimensional slice, the electron density of an object by collecting radiation emitted from an external source and scattered throughout this object. The collected data at specific scattering energies appears essentially as the integral of the electron density on definite families of arcs of circles. Reconstruction of the unknown electron density is achieved by the inversion of the corresponding circular-arcs Radon transforms (CART). We review two existing CST modalities, their corresponding CART and establish their numerical inversion algorithms in the formalism of the so-called circular harmonic decomposition (CHD) for a function. The quality of the reconstructed images is illustrated by numerical simulations on test phantoms. Comparison with standard tomography performances demonstrates the efficiency and interest of this inversion method via CHD in imaging science such as biomedical imaging and non-destructive industrial testing.

Keywords: compton scattering tomography; inverse problems; numerical algorithm; biomedical imaging; non-destructive testing

AMS Subject Classifications: 92C55 Biomedical imaging and signal processing; 44A12 Radon Transform; 65R10 Integral transforms; 65J22 Inverse problems

1. Introduction

Conventional tomography (X-ray scanner, Single Photon Emission Computed Tomography, Positron Emission Tomography, etc.) is widely used in numerous fields such as biomedical imaging, non-destructive industrial testing, environmental survey, etc. In these tomographies, only primary radiation is used for imaging whereas Compton scattered radiation is considered as noise reducing image quality. Therefore, the effects of scattered radiation are routinely eliminated or at least compensated for [1].

However, one may turn the problem around and ask whether scattered radiation may be used as an imaging agent. This point of view has been advocated since the middle of the last century in medical imaging as well as in industrial control [2–5]. The idea has many highly desirable features. In the field of diagnostic medical imaging, radiography using scattered radiation could provide a direct and quantitative measurement of the density of

*Corresponding author. Email: mai.nguyen-verger@u-cergy.fr

ISSN 1741–5977 print/ISSN 1741–5985 online

http://dx.doi.org/10.1080/17415977.2011.653008
http://www.tandfonline.com

the studied object. In non-destructive testing, three advantages can be pointed out. It permits to place both the radiation source and the detector on the same side of the object. It has also greater sensitivity to low-density materials such as gases. Finally, it allows direct spatial definition with high contrast resolution.

In this work we shall focus on Compton scattering tomography (CST), an imaging principle which makes use of integral measurements. There are at least two such CST modalities: Norton's [6] and ours proposed in 2010 [7] where the measurements are modelled by Radon transforms on definite families of arcs of circles. Image reconstruction amounts to inverting the corresponding circular-arc Radon transform (CART).

Since the seminal work of Radon [8], many extensions of this integral transform have been widely discussed, in particular in the literature of imaging science. This is the case when the results of measurements appear under the form of integrals of a physical quantity over lower dimensional manifolds. The relevant problem to solve is the recovery of the physical quantity of interest as a function in $\mathbb{R}^2$.

In 1981, Cormack [9,10] studied Radon transforms on two remarkable families of curves in the plane defined by

$$r^{\alpha}\cos(\alpha(\theta-\varphi)) = p^{\alpha}, \quad \text{with } |\theta-\varphi| \leq \frac{\pi}{2\alpha},$$

in the case of the α-curves ($\alpha > 0$) and by

$$p^{\beta}\cos(\beta(\theta-\varphi)) = r^{\beta}, \quad \text{with } |\theta-\varphi| \leq \frac{\pi}{2\beta},$$

in the case of the β-curves ($\beta > 0$). Cormack was able to show several properties of the circular harmonic components of the Radon transforms on these two classes of curves and has established an inversion formula in terms of the circular harmonic components of the unknown function.

Then he derived a consistency condition for the data which permits to regularize the inverse formulas. From the regularized formulas, Chapman and Cary [11] discussed an alternative inversion algorithm to the 'Filtered Back-Projection' (FBP) algorithm for the standard Radon transform (RT) and showed that the fulfilment of the consistency criterion of the data reduces the number of artefacts. This is not so in the well-known FBP algorithm.

In 1994, Norton [6] proposed a Compton scattering tomographic device in which the primary radiation point-source (S) is fixed and the point-like detector (D) moves along a straight line passing through the point-source. Norton showed that integral data collected on isogonal arcs of circle can be useful for image reconstruction if they are identified with an RT on arcs of circle passing through a fixed point (S). We shall call it CART_1. Norton gave an inversion formula for the CART_1 via the so-called FBP algorithm ($CART_1 - FBP$).

On the other hand, the CART_1 is precisely the RT defined on the $\beta = 1$-curves and admits readily an analytic inverse as shown by Cormack [9]. In this article, we develop a new numerical inversion procedure via circular harmonic decomposition for the CART_1 ($CART_1 - CHD$) and compare it to Norton's FBP algorithm ($CART_1 - FBP$).

Moreover, in 2010 we have proposed a new CST modality [7] in which the segment source-detector (SD) rotates around its middle point and the integral data collected on isogonal arcs of circle are adequately modelled by an RT on circular arcs of circle which subtend a chord of fixed length and rotate around its middle point. This new RT

(called circular-arc Random transform ($CART_2$)) can be viewed as the RT on the ($\alpha = 1$)-curves after a change of functions. The $CART_2$ requires to work in polar coordinates and since the circular harmonic decomposition (CHD) is adapted to a polar approach, the inversion procedure can be advantageously made in the circular harmonic domain. This is why, we develop a new numerical inversion algorithm for $CART_2$ in the CHD framework ($CART_2 - CHD$).

In this article we review two modalities in CST: Norton's device (CST_1) and ours (CST_2), and the two corresponding circular-arcs RT: $CART_1$ and $CART_2$ for Norton's case and ours, respectively. The novelty in this work is the development of two numerical inversions via CHD for two circular-arcs RTs ($CART_1$ and $CART_2$) for the first time. Until now, the CHD approach has not been widely used for image reconstruction. However, this approach offers many advantages, in particular in the case of Radon data [9–11], for example consistency between the image reconstruction formula and the data, stable algorithms, reduced artefacts, less complexity in algorithms and less computing time.

This article is organized as follows. Section 2 reviews the working principle of Norton's CST modality and the associated $CART_1$. Section 3 reviews our CST and the corresponding $CART_2$. In Section 4 the novel numerical inversion via CHD for $CART_1$ is developed and compared to Norton's FBP algorithm. In Section 5 the numerical inversion for $CART_2$ is worked out and image reconstruction in CST_2 is compared with those obtained in conventional tomography modelled by the classical RT and computed by the FBP algorithm ($RT - FBP$). Section 6 deals with the attenuation correction and the robustness to the Poisson noise in our two transforms. Finally, a conclusion and research perspectives are presented in the last section.

2. Norton's CST_1 and RT defined on arcs of circles passing through a fixed point ($CART_1$)

2.1. *Working principle and Norton's inversion method*

Norton [6] worked out a CST modality which is based on an RT on circles having a fixed common point. The working principle is given by Figure 1. A point source **S** emits primary radiation towards an object defined by its electron density function $n_e(r, \theta)$, of which **M** is a scattering site (running point).

A point detector **D** moves along an Ox-axis and collects, at given energy E, scattered radiation from the object. The physics of Compton scattering demands that the registered radiation flux density g at site **D** is due to the contribution of all scattering sites **M** lying on an arc of circle from **S** to **D** subtending an angle ($\pi - \omega$), where ω is the scattering angle corresponding to the outgoing energy E, as given by the Compton formula:

$$E = \frac{E_0}{1 + \frac{E_0}{mc^2}(1 - \cos\omega)}, \tag{1}$$

where E_0 is the emitted photon energy and mc^2 represents the energy of an electron at rest (0.511 MeV).

Norton gave the expression of the projections g as:

$$g(\rho, \varphi) = \int_{\varphi - \pi/2}^{\varphi + \pi/2} \mathrm{d}\theta \int_{-\infty}^{\infty} \mathrm{d}r\, 2\rho n_e(r, \theta) w(r, \theta; \rho, \varphi) \times \delta[r - 2\rho\cos(\theta - \varphi)], \tag{2}$$

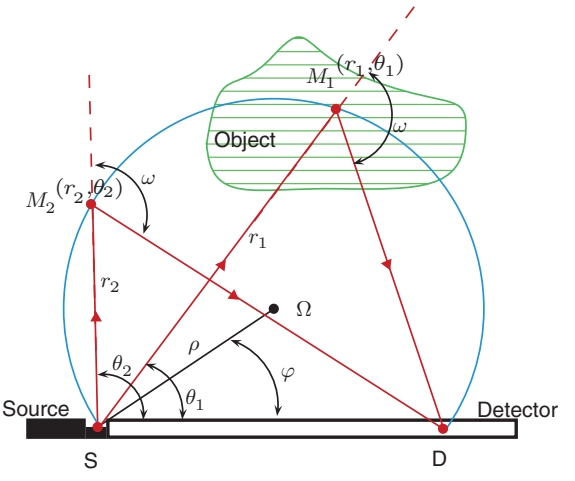

Figure 1. Principle of Norton's CST (CST_1).

where $\delta(\cdot)$ is the Dirac delta function concentrated on a circular-arc of equation $r = 2\rho\cos(\theta - \varphi)$ and $w(\cdot)$ is defined by:

$$w(r,\theta;\rho,\varphi) = \frac{ars(\theta)P(\varphi + \pi/2)}{4\pi(2\rho)^4 \sin^2\theta}.$$

In the above equation, a represents the area of an element of detection, $s(\theta)$ expresses any angular dependence of the gamma-ray source distribution and $P(\omega)$ (where $\omega = \pi/2 + \varphi$) is the Klein–Nishina differential cross section,

$$P(\omega) = \frac{r_e^2}{2}\frac{1}{1+\epsilon(1-\cos\omega)^2}\left(1+\cos^2\omega + \frac{\epsilon^2(1-\cos\omega)^2}{1+\epsilon(1-\cos\omega)}\right) \quad \text{with} \quad \epsilon = \frac{E_0}{mc^2}.$$

Mathematically, g is essentially the RT of the object electron density $n_e(M)$ on arcs of circle ($CART_1$), when radiation attenuation and photoelectric effects on radiation propagation are neglected.

Norton gave an inverse formula

$$n_e(r,\theta) = \frac{1}{\pi^2}\int_0^{2\pi} d\varphi \int_0^{\infty} d\rho \frac{g(\rho,\varphi)}{w(r,\theta;\rho,\varphi)}\, h[r - 2\rho\cos(\theta-\varphi)],$$

where

$$h(x) = \int_{-\infty}^{\infty} e^{-i\zeta x}|\zeta| d\zeta. \tag{3}$$

Following Norton, Equation (3) is the same convolution kernel employed in the FBP algorithm used in X-ray transmission computed tomography (CT). The difference is that the Back-Projection is performed along straight lines in transmission CT, whereas here this is performed along the circles $r = 2\rho\cos(\theta - \varphi)$ (we call it $CART_1 - FBP$ in Subsection 4.2).

The image reconstruction in the Norton's case amounts to calculating this FBP associated to the $CART_1$. Nevertheless, we will study the $CART_1$ in a new way via CHD in Section 2.2 and propose an alternative numerical inversion method in Section 4.

2.2. *Radon transform on arcs of circle through a fixed common point ($CART_1$) and CHD*

We start from Equation (2). Let:

$$\begin{cases} \mathcal{C}^1 f(\rho,\varphi) = g(\rho,\varphi)\dfrac{(2\rho)^4}{P(\varphi+\pi/2)} \\ f(r,\theta) = n_e(r,\theta)\dfrac{as(\theta)r}{4\pi\sin^2\theta} \\ p = 2\rho. \end{cases} \tag{4}$$

Substituting Equation (4) into (2), we obtain

$$\mathcal{C}^1 f(p,\varphi) = \int_{\varphi-\pi/2}^{\varphi+\pi/2} \mathrm{d}\theta \int_{-\infty}^{+\infty} \mathrm{d}r p f(r,\theta)\delta\big\{r - p\cos(\theta-\varphi)\big\}. \tag{5}$$

This equation gives the integral of a function $f(r,\theta)$ on a class of circles having a fixed common point ($CART_1$) and defined by the delta function integral kernel in (r,θ)-space.

This equation belongs to the β-curve ($\beta=1$) family [9] and so is suitable for circular harmonic decomposition. This is why, the inverse transform can be worked out using the Fourier angular components of f and $\mathcal{C}^1 f$:

$$\begin{cases} f(r,\theta) = \displaystyle\sum_{l\in\mathbb{Z}} f_l(r)e^{il\theta} \\ \text{with} \\ f_l(r) = \dfrac{1}{2\pi}\displaystyle\int_0^{2\pi} f(r,\theta)e^{-il\theta}\mathrm{d}\theta \end{cases} \quad \text{and} \quad \begin{cases} \mathcal{C}^1 f(p,\varphi) = \displaystyle\sum_{l\in\mathbb{Z}} \mathcal{C}^1 f_l(p)e^{il\varphi} \\ \text{with} \\ \mathcal{C}^1 f_l(p) = \dfrac{1}{2\pi}\displaystyle\int_0^{2\pi} \mathcal{C}^1 f(p,\varphi)e^{-il\varphi}\mathrm{d}\varphi. \end{cases} \tag{6}$$

In terms of Fourier angular components of f and $\mathcal{C}^1 f$, Equation (5) becomes

$$\mathcal{C}^1 f_l(p) = 2\int_0^p f_l(r)\frac{\cos\left[l\cos^{-1}\left(\frac{r}{p}\right)\right]}{\sqrt{1-\left(\frac{r}{p}\right)^2}}\mathrm{d}r. \tag{7}$$

Equation (7) is precisely the integral equation for f_l in the case of a ($\beta=1$)-curve of Cormack [9,10]. Thanks to a consistency condition on the data, he could derive the regularized inverse formula for this circular RT expressed in terms of circular harmonic components:

$$f_l(r) = \frac{1}{\pi r}\int_0^r \frac{e^{-|l|\cosh^{-1}(r/p)}}{\sqrt{(\frac{r}{p})^2-1}}\big(\mathcal{C}^1 f_l\big)'(p)\mathrm{d}p - \frac{1}{\pi r}\int_r^{+\infty} U_{|l|-1}(r/p)\big(\mathcal{C}^1 f_l\big)'(p)\mathrm{d}p, \tag{8}$$

where $U_{l-1}(\cos x) = \sin lx/\sin x$ is the Chebyshev polynomial of second kind. $(\mathcal{C}^1 f_l)'$ is the derivative of $\mathcal{C}^1 f_l$ with respect to p. Finally, $f(r,\theta)$ is reconstructed through its Fourier expansion with the circular harmonic components $f_l(r)$. Thus the recovery of the electron

density function $n_e(r,\theta)$ in Norton's CST is achieved by a change of functions given in Equation (4). In Section 4, we will establish a numerical algorithm to compute $f_l(r)$.

3. Novel CST modality (CST_2) and RT on arcs of circle with a chord of fixed length and rotating around its middle point ($CART_2$)

3.1. *Working principle*

Consider a two-dimensional object represented by a non-negative continuous function $f(\mathbf{M})$ with bounded support in $\mathbb{R}^2$. An emitting point source **S** is placed at a distance $2p$ from a point detector **D**. We consider only the upper part of space. This is possible because an angle collimator is placed at **D**. The segment **SD** rotates around its middle point **O** and its angular position is given by φ.

Emitted photons are scattered at site **M** and some of them are detected by the detector **D** at an energy E_ω. Therefore the detector can record scattered photons according to scattered energy which is related to the scattering angle ω by the Compton formula. Thus, for a fixed φ, to each energy E_ω corresponds a set of scattering sites on a circular arc $\mathscr{C}(\omega,\varphi)$.

Figure 2 shows the scanning of the studied medium in this new CST modality at different energies E_ω or at different scattering angles ω. The set of scattering sites for given ω is an isogonal circular arc $\mathscr{C}(\omega,\varphi)$ passing through the pair (**S**, **D**).

The modelling of this novel modality in CST leads us to study the integral of a function on a class of circular arcs (different from the one in $CART_1$). This is the new RT defined on circular arcs called $CART_2$ [7].

3.2. *$CART_2$ and CHD*

We consider a new class of circles of radius R, which have a common chord of length $2p$ making an angle $(\varphi-\frac{\pi}{2})$ with the Ox-axis (Figure 3). A point of the circle with polar coordinates (r,θ) satisfies the following equation:

$$r^2+2r\sqrt{R^2-p^2}\cos(\theta-\varphi)-p^2=0. \tag{9}$$

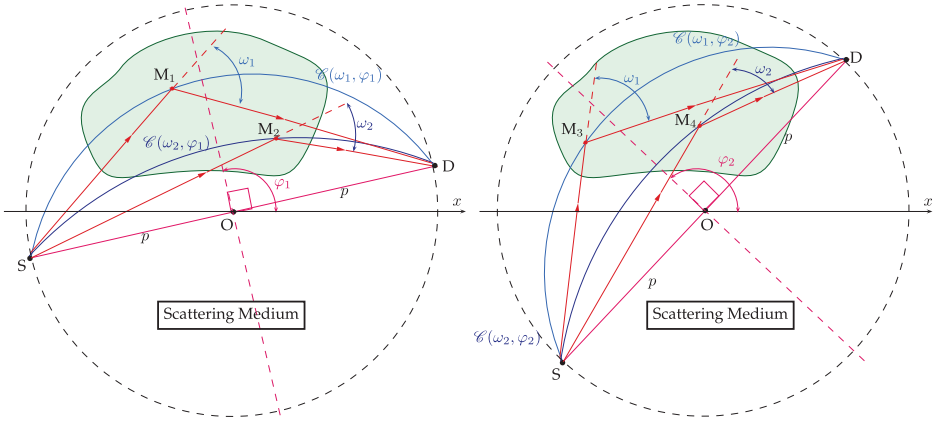

Figure 2. Scanning of the studied object.

A close inspection reveals that the circular arc SD of Figure 3 is the arc that subtends a subscribed angle $(\pi-\omega)$. Thus putting $\tau=\cot\omega$, we have $\sqrt{R^2-p^2}=p\tau$ and we can rewrite Equation (9) as the following polar equation $r(\theta)$:

$$r=p(\sqrt{1+\tau^2\cos^2\gamma}-\tau\cos\gamma), \tag{10}$$

where $\gamma=\theta-\varphi$ and with $(\omega,\varphi)\in]0,\frac{\pi}{2}]\times[0,2\pi]$, which defines the curve $\mathscr{C}(\tau,\varphi)$. The RT $\mathcal{C}^2f(\varphi,\tau)$ of a function $f(r,\theta)$ on a curve $\mathscr{C}(\tau,\varphi)$ is given by:

$$\mathcal{C}^2f(\varphi,\tau)=\int_{(r,\theta)\in\mathscr{C}(\tau,\varphi)}f(r,\theta)\mathrm{d}s, \tag{11}$$

where $\mathcal{C}^2$ is the CART_2 established in (φ,τ)-space and $\mathrm{d}s$ is the elementary length of circular arc to be computed from the circular-arc Equation (10):

$$\mathrm{d}s=r\,\mathrm{d}\gamma\sqrt{\frac{1+\tau^2}{1+\tau^2\cos^2\gamma}}=\mathrm{d}r\,\frac{\sqrt{1+\tau^2}}{\tau\sin\gamma}. \tag{12}$$

Substituting (12) into (11), we obtain an explicit form of the integral of a function $f(r,\theta)$ on a curve $\mathscr{C}(\tau,\varphi)$ in terms of γ:

$$\mathcal{C}^2f(\varphi,\tau)=\int_{-\frac{\pi}{2}}^{\frac{\pi}{2}}f(r(\gamma),\gamma+\varphi)r(\gamma)\frac{\sqrt{1+\tau^2}}{\sqrt{1+\tau^2\ \cos^2\gamma}}\mathrm{d}\gamma. \tag{13}$$

Thus Equation (13) describes the image formation process.

Rotational invariance around the coordinate origin suggests a Fourier series angular expansion, this is why the inverse transform can be worked out using the Fourier angular components of f and $\mathcal{C}^2f$:

$$\begin{cases} f(r,\theta)=\displaystyle\sum_{l\in\mathbb{Z}}f_l(r)e^{il\theta} \\ \text{with} \\ f_l(r)=\dfrac{1}{2\pi}\displaystyle\int_0^{2\pi}f(r,\theta)e^{-il\theta}\mathrm{d}\theta \end{cases} \quad\text{and}\quad \begin{cases} \mathcal{C}^2f(\varphi,\tau)=\displaystyle\sum_{l\in\mathbb{Z}}\mathcal{C}^2f_l(\tau)e^{il\varphi} \\ \text{with} \\ \mathcal{C}^2f_l(\tau)=\dfrac{1}{2\pi}\displaystyle\int_0^{2\pi}\mathcal{C}^2f(\varphi,\tau)e^{-il\varphi}\mathrm{d}\varphi. \end{cases} \tag{14}$$

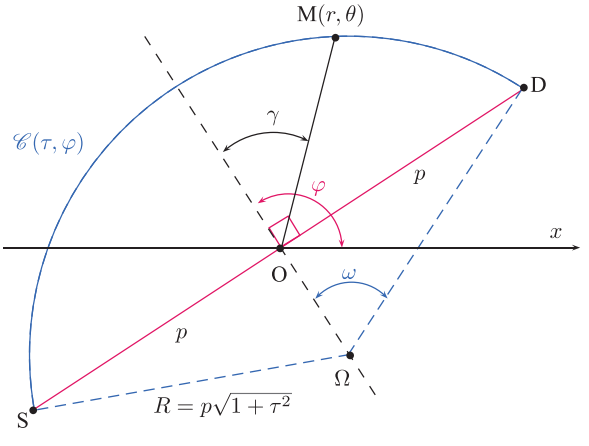

Figure 3. Representation of the curve $\mathscr{C}(\tau,\varphi)$.

Following [7], we give an integral equation linking $\mathcal{C}^2 f_l(\tau)$ to $f_l(r)$, the circular components of $\mathcal{C}^2 f(\varphi, \tau)$ and $f(r, \theta)$. Since $\gamma = \theta - \varphi$ and accounting for the invariance of the integrand under $\gamma \longleftrightarrow -\gamma$, Equation (13) takes the form

$$\mathcal{C}^2 f_l(\tau) = 2 \int_0^{\frac{\pi}{2}} r(\gamma) \frac{\sqrt{1+\tau^2}}{\sqrt{1+\tau^2\cos^2(\gamma)}} f_l(\gamma) \cos(l\gamma) \mathrm{d}\gamma. \tag{15}$$

Because of the equation of the circular arc (Equation (10)), we can show that

$$\mathrm{d}\gamma \frac{r(\gamma)}{\sqrt{1+\tau^2\cos^2\gamma}} = \frac{\mathrm{d}r}{\sqrt{\tau^2 - \frac{1}{4}\left(\frac{p}{r} - \frac{r}{p}\right)^2}}.$$

Now using this relationship between the differential elements, we change back to the r-variable equation (15) to obtain

$$\frac{\tau \mathcal{C}^2 f_l(\tau)}{\sqrt{1+\tau^2}} = 2 \int_{p(\sqrt{1+\tau^2}-\tau)}^{p} \frac{\cos\left[l \cos^{-1}\left(\frac{1}{2\tau}\left(\frac{p}{r} - \frac{r}{p}\right)\right)\right]}{\sqrt{1 - \frac{1}{4\tau^2}\left(\frac{p}{r} - \frac{r}{p}\right)^2}} f_l(r) \mathrm{d}r. \tag{16}$$

This new form is adapted to Cormack's inversion procedure [9], with the following change of variables [7]:

$$q = \frac{1}{\tau} = \tan\omega, \quad \text{and} \quad t^{-1} = \frac{1}{2}\left(\frac{p}{r} - \frac{r}{p}\right).$$

Then we apply the Cormack's procedure [9], see also [12], to invert Equation (16) and obtain the inverse transform of the CART_2 through the circular harmonic decomposition:

$$f_l(r) = (-)\frac{2p(p^2+r^2)}{\pi(p^2-r^2)^2}\left[\int_t^{\infty} \frac{\cosh(l\cosh^{-1}(\frac{q}{t}))}{\sqrt{q^2-t^2}} \frac{\mathrm{d}}{\mathrm{d}q}\left(\frac{\mathcal{C}^2 f_l(\frac{1}{q})}{\sqrt{1+q^2}}\right)\mathrm{d}q\right]_{t=\frac{2pr}{p^2-r^2}}. \tag{17}$$

Finally, $f(r, \theta)$ is reconstructed through its Fourier expansion with the circular harmonic components $f_l(r)$. We have given the forward and inverse transforms in the case of this new CST modality. In Section 5, we will develop the numerical inversion procedure for image reconstruction.

4. Numerical inversion via CHD for CART_1

4.1. *Computation of inverse CART_1*

We will now establish a numerical approach to compute the CART_1 in Equation (8). First, we make the change of variable $r = p\cosh(\chi)$ in the first integral and $r = p\cos(\chi)$ in the second one. The transform (8) becomes

$$\begin{aligned} f_l(r) = \frac{1}{\pi}\int_0^{\cosh^{-1}\left(\frac{r}{p_{\min}}\right)} \frac{e^{-|l|\chi}}{\cosh^2\chi}\left(\mathcal{C}^1 f_l\right)'\left(\frac{r}{\cosh\chi}\right)\mathrm{d}\chi \\ - \frac{1}{\pi}\int_0^{\cos^{-1}\left(\frac{r}{p_{\max}}\right)} \frac{\sin(|l|\chi)}{\cos^2\chi}\left(\mathcal{C}^1 f_l\right)'\left(\frac{r}{\cos\chi}\right)\mathrm{d}\chi. \end{aligned} \tag{18}$$

To simplify the algebra and notation, we consider that p and r have the same sampling Δr. So we can define the discretized forms of $f_l(r)$ and $g_l(p) = C^1 f_l(p)$ as

$$g_{lk} = g_l(k\Delta r) \quad \text{and} \quad f_{lj} = f_l(j\Delta r),$$

where $(j,k) \in [1,K]^2$ with $K = \frac{\Delta r}{p_{\max}}$. Moreover, we use linear interpolation to simplify the algorithm and the calculation of the derivative of the data g_l. So in the interval $k\Delta r < p < (k+1)\Delta r$, we can write

$$\bar{g}_{lk} = \frac{g_{l(k+1)} - g_{lk}}{\Delta r}.$$

Finally, we obtain a discretized form of Equation (18) :

$$f_{lj} = -\frac{1}{\pi}\left[\sum_{k=1}^{j-1} \bar{g}_{lk}\left(J_l(\chi_{j(k+1)}) - J_l(\chi_{jk})\right) + \sum_{k=j}^{K-1} \bar{g}_{lk}\left(I_l(\chi_{j(k+1)}) - I_l(\chi_{jk})\right)\right], \tag{19}$$

in terms of the primitive integrals :

$$I_l(\chi_{jk}) = \int^{\chi_{jk}} \frac{\sin(|l|x)}{\cos^2 x}\mathrm{d}x \quad \text{and} \quad J_l(\chi_{jk}) = \int^{\chi_{jk}} \frac{e^{-|l|x}}{\cosh^2 x}\mathrm{d}x. \tag{20}$$

The variables χ_{jk} corresponds to the discrete radii $p = k\Delta r$

$$\chi_{jk} = \begin{cases} \cosh^{-1}\left(\dfrac{j}{k}\right) & \text{for } 1 \le k \le j \\ \cos^{-1}\left(\dfrac{j}{k}\right) & \text{for } j \le k \le K. \end{cases}$$

We evaluate the primitive integrals (20) using the recurrence relation:

$$\forall n > 2, \quad I_n(x) = \frac{2}{n-2}(\tan x \sin((n-2)x) - \cos((n-2)x)) - \frac{n}{n-2} I_{n-2}(x),$$

with the initial conditions :

$$I_1(x) = \frac{1}{\cos x} \quad \text{and} \quad I_2(x) = -2\ln(\cos x).$$

In the same way, we make the change of variable $u = e^{\chi_{jk}}$ in the second primitive and we let $n = |l| - 1$:

$$J_n(u) = \int \frac{\mathrm{d}u}{u^n(u^2+1)^2}.$$

So we obtain the following recurrence relation:

$$\forall n > 1, \quad J_{n+1}(u) = -\frac{1}{nu^n(u^2+1)} - \frac{n+2}{n} J_{n-1}(u),$$

with the initial conditions:

$$J_0(u) = \frac{u}{2(u^2+1)} + \frac{1}{2}\arctan(u) \quad \text{and} \quad J_1(u) = -\frac{1}{2}\ln(u^2+1) + \ln(u) + \frac{1}{2(u^2+1)}.$$

We also have the special case $l=0$. For this case, we evaluate the primitive integral $J_0(\chi_{jk})$ as

$$J_0(\chi_{jk}) = \int^{\chi_{jk}} \frac{1}{\cosh^2 x}\,\mathrm{d}x = \frac{\sinh \chi_{jk}}{\cosh \chi_{jk}} = \sqrt{1-\left(\frac{k}{j}\right)^2},$$

hence,

$$f_{0j} = -\frac{1}{\pi}\sum_{k=1}^{j-1} \bar{g}_{0k}\left(\sqrt{1-\left(\frac{k+1}{j}\right)^2} - \sqrt{1-\left(\frac{k}{j}\right)^2}\right).$$

So, we obtained all the f_{lj}, which is the discretized form of circular components $f_l(r)$. Finally, we work out the summation $f_l(r)$ to obtain the original function $f(r,\theta)$.

We have established an algorithm via CHD for the inverse CART_1 ($CART_1 - CHD$). This is an alternative to the $CART_1 - FBP$ algorithm proposed by Norton for the CST_1.

We therefore set up the following image reconstruction scheme and apply it to the reconstruction of a point source (Figure 4).

4.2. *Simulation results: image reconstructions by $CART_1 - CHD$ and by $CART_1 - FBP$*

In this section, we present the numerical simulation of the circular RT $CART_1$ applied on the Shepp–Logan medical phantom (Figure 5) and on a nuclear waste image (Figure 6). The source is placed below on the left of the image and the detector moves along the axis Sx. The scattering medium is discretized with 256×256 of length units (pixels). We consider the number of rotational positions N_φ and the number of radii N_p. These numbers define the corresponding sampling steps $\mathrm{d}\varphi$ and $\mathrm{d}p$ by:

$$\mathrm{d}\varphi = \frac{2\pi}{N_\varphi} \quad \text{and} \quad \mathrm{d}p = \frac{4*256}{N_p}.$$

We take $N_\varphi = N_p = 4*256$. As the system of the corresponding CST_1 does not rotate around the object, the (φ,p)-space is very large in front of the studied image. So to 'well-observe' the object, we have to take a large maximum value of p (4 times the image size).

To illustrate and compare the quality of the reconstructions, we define the normalized mean square error ($NMSE$) and the normalized mean absolute error ($NMAE$) (expressed as a percentage):

$$NMSE = \frac{100}{N^2}\frac{\sum_{(i,j)\in[1,N]^2}\left|\mathcal{I}_r(i,j)-\mathcal{I}_o(i,j)\right|^2}{\max_{(i,j)\in[1,N]^2}\{\mathcal{I}_o(i,j)\}^2}$$

and

$$NMAE = \frac{100}{N^2}\frac{\sum_{(i,j)\in[1,N]^2}\left|\mathcal{I}_r(i,j)-\mathcal{I}_o(i,j)\right|}{\max_{(i,j)\in[1,N]^2}\{\mathcal{I}_o(i,j)\}},$$

where $\mathcal{I}_r$ is the reconstructed image and $\mathcal{I}_o$ is the original image.

The image reconstructions by $CART_1 - CHD$ are compared with the ones obtained by Norton's $CART_1 - FBP$.

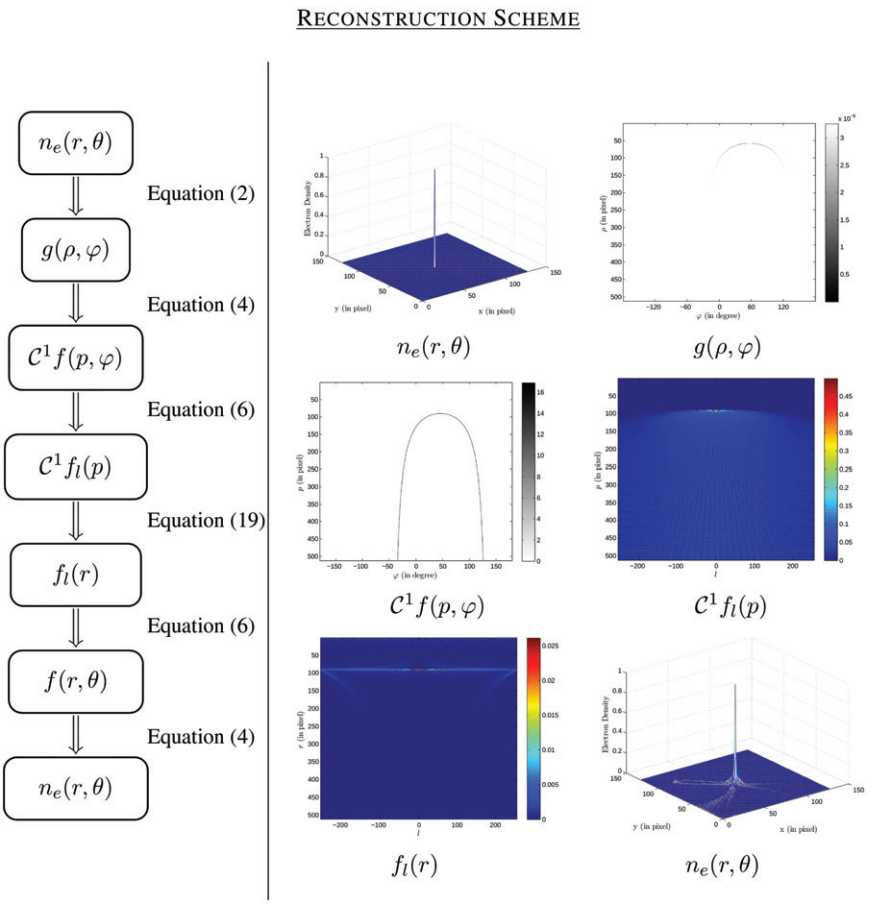

Figure 4. Inversion procedure of the CART_1 and its illustration for the reconstruction of a point object.

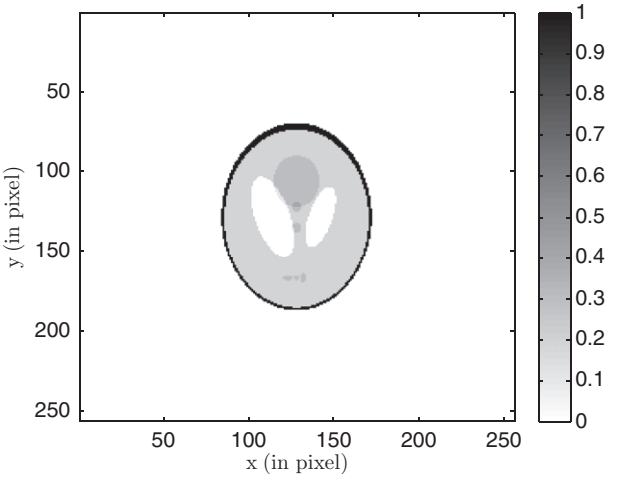

Figure 5. Original of the Shepp–Logan phantom of size 128×128.

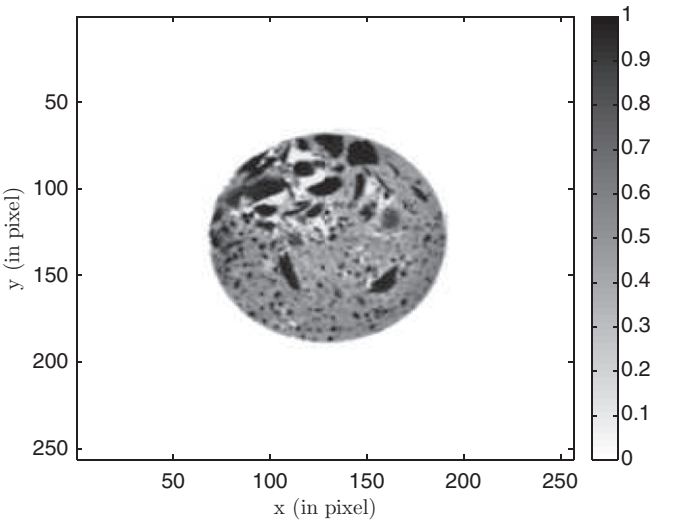

Figure 6. Original of the nuclear waste.

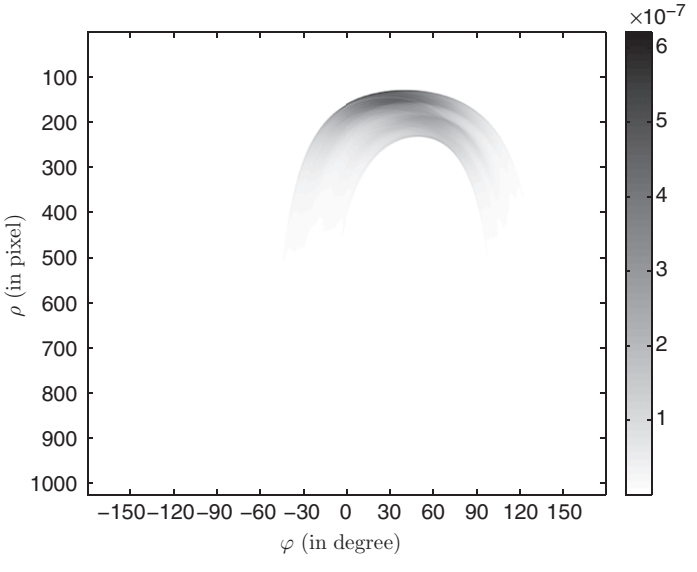

Figure 7. CART_1 of the Shepp–Logan phantom shown in Figure 5.

To erase the artefacts generated around the object by the circular harmonic decomposition approach, we can use information given by the contours of the projections. If projections are equal to zero, then the corresponding circular-arc does not cross the object. Therefore assuming that the object of interest is bounded in a closed space, a null set in the projection space corresponds to a null set in the original space.

Figures 7 and 8 show the forward CART1 of the Shepp-Logan phantom and of the nuclear waste. The $CART_1 - CHD$ approach gives a very interesting image quality in the reconstruction of the Shepp–Logan phantom (Figure 9) and of the nuclear waste

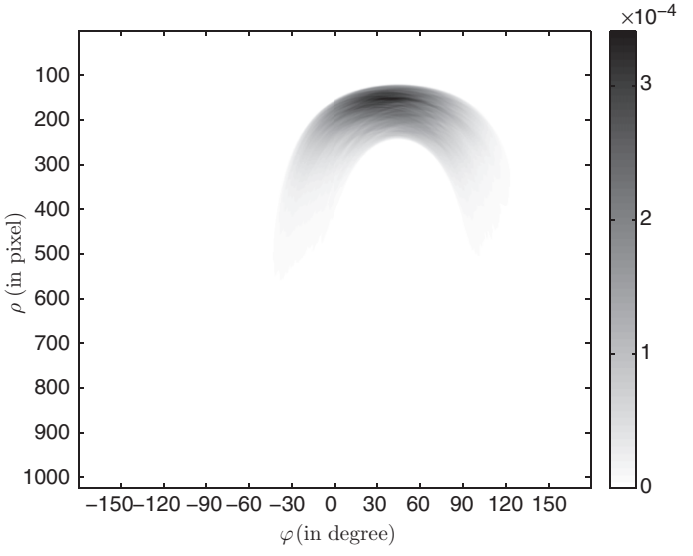

Figure 8. CART_1 of the the nuclear waste shown in Figure 6.

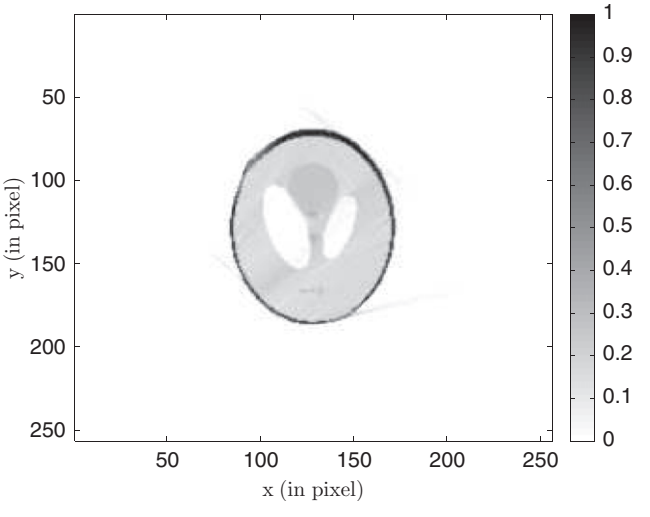

Figure 9. Reconstruction of the Shepp–Logan phantom shown in Figure 5 using $CART_1 - CHD$ and data in Figure 7 with NMAE = 0.83% and NMSE = 0.16%.

(Figure 10). Indeed, contours and small structures are better recovered than with the Norton's inverse formula (Figures 11 and 12). Nevertheless, the form of the artefacts is different in two cases: a circular form for the $CART_1 - CHD$ and a quasi-homogeneous form for the $CART_1 - FBP$. Moreover $p \in \mathbb{R}^+$, but we have to fix a maximum value $p_{\max}$ for numerical computation, such that a sharp cut-off of p and the loss of data generate significant artefacts whereas the ramp filter in $CART_1 - FBP$ is apodized. To reduce the artefacts in our case, we have to increase $p_{\max}$ and therefore increase the length of the detector in the related CST_1.

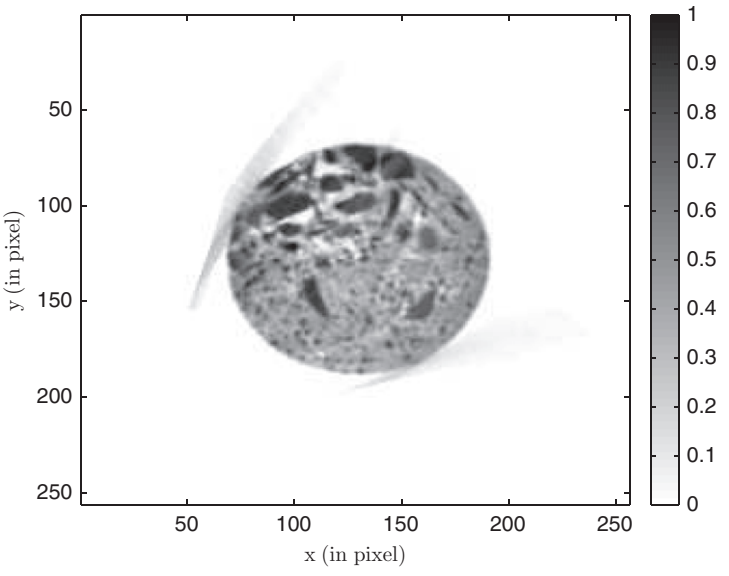

Figure 10. Reconstruction of the nuclear waste shown in Figure 6 using $CART_1 - CHD$ and data in Figure 8 with NMAE = 2.09% and NMSE = 0.28%.

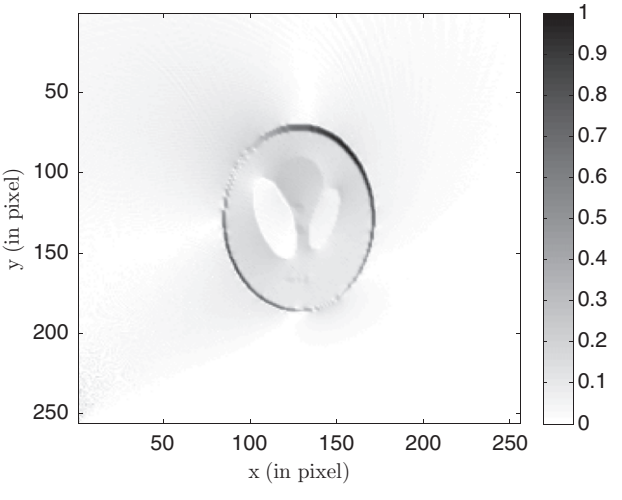

Figure 11. Reconstruction of the Shepp–Logan phantom shown in Figure 5 using $CART_1 - FBP$ and data in Figure 7 with NMAE = 3.6% and NMSE = 0.5%.

The numerical error measurements obtained using the $CART_1 - CHD$ are smaller as compared to those of the Norton's inverse formula and prove the efficiency of this algorithm.

The main aim of this work is to establish a new imaging principle by Compton scattered radiation. This is why other factors in realistic imaging systems are not treated here, such as medium attenuation and Poisson emission noise.

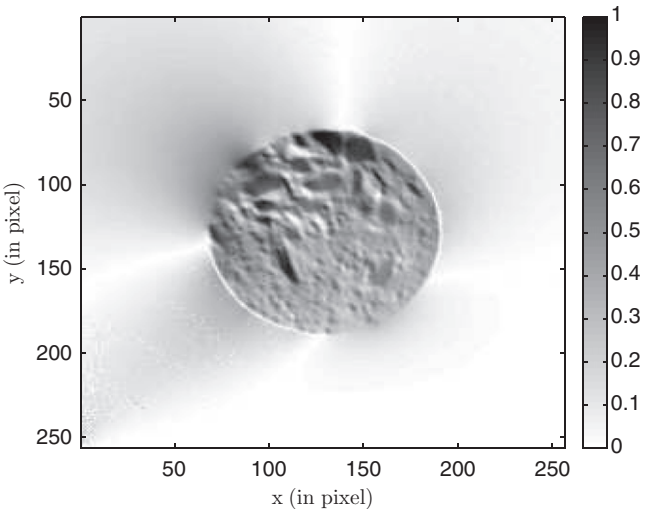

Figure 12. Reconstruction of the nuclear waste shown in Figure 6 using $CART_1 - FBP$ and data in Figure 8 with NMAE = 10.4% and NMSE = 1.6%.

5. Numerical inversion via CHD for $CART_2$

5.1. *Regularization procedure and reconstruction scheme*

In principle, one can use Equation (17) to perform numerical computations. However, assuming that the original function is bounded, a close inspection of the integral kernel of Equation (17) shows that it behaves as

$$\lim_{q\to+\infty} \frac{\cosh(l\ \cosh^{-1}(\frac{q}{t}))}{q\sqrt{(\frac{q}{t})^2-1}} \approx \lim_{u\to+\infty} 2\ e^{(|l|-2)u}, \tag{21}$$

where $u = \cosh^{-1}(\frac{q}{t})$. Equation (21) presents an apparent divergence when $|l| > 2$, since for $q \to \infty$ the integrand grows very rapidly. This explains that when $|l| > 2$, this apparent divergence makes the q-integral unstable, and as such the presence of noise in the data $\mathcal{C}^2 f_l(1/q)$ for large q is badly propagated into the calculation of $f_l(r)$ which prevents simulation studies. It then becomes obvious that Equation (17) needs to be regularized.

Even if the circular arc doesn't belong to the α-curves family (defined by Cormack [9]), we will see that there is a frequential link between them. Indeed, by introducing:

$$F_l\left(t = \frac{2pr}{p^2-r^2}\right) = \frac{(p^2-r^2)^2}{2p(p^2+r^2)} \times f_l(r) \quad \text{and} \quad G_l(q) = \frac{\mathcal{C}^2 f_l(\frac{1}{q})}{\sqrt{1+q^2}}, \tag{22}$$

we obtain:

$$F_l(t) = (-)\frac{1}{\pi}\int_t^\infty \mathrm{d}q \frac{\cosh(l\cosh^{-1}(q/t))}{\sqrt{q^2-t^2}} \frac{\mathrm{d}G_l(q)}{\mathrm{d}q}\bigg|_{t=\frac{2pr}{p^2-r^2}}. \tag{23}$$

Equation (23) is precisely the straight-line RT inversion formula in (q, t)-space given by Cormack's regularization procedure. Thus with two changes of functions (Equation (22)), we pass from the original space of the $CART_2$ definition to a new space in which the

CART_2 becomes the ordinary RT. Cormack proposed a regularization procedure based on consistency conditions of the circular harmonic components of the data

$$\int_0^\infty \mathrm{d}q \ \frac{\mathrm{d}G_l(q)}{\mathrm{d}q} q^{\alpha_l} = 0 \quad \text{for } \alpha_l = (l-1), (l-3), \ldots, > 0.$$

Thanks to these conditions and the identity of the Chebyshev polynomial linking the polynomial of first kind ($T_l(\cdot)$) to the second kind Chebyshev polynomial ($U_l(\cdot)$)

$$\frac{T_l(x)}{\sqrt{x^2-1}} = \frac{\left(x-\sqrt{x^2-1}\right)^l}{\sqrt{x^2-1}} + U_{l-1}(x),$$

the following regularized inverse formula for the CART_2 can be derived

$$F_l(t) = \frac{1}{\pi t}\int_0^t \mathrm{d}q G_l'(q) U_{|l|-1}\left(\frac{q}{t}\right) - \frac{1}{\pi t}\int_t^\infty \mathrm{d}q G_l'(q) \frac{\left((q/t)-\sqrt{(q/t)^2-1}\right)^{|l|}}{\sqrt{(q/t)^2-1}}. \tag{24}$$

where $t = \frac{2pr}{p^2-r^2}$ and $U_{l-1}(\cos x) = \sin lx / \sin x$. This formula will be used in our simulations.

We therefore set up the following reconstruction scheme and apply it to the reconstruction of a point source (Figure 13).

5.2. *Computation of the inverse CART₂*

Then we follow the Chapman and Cary computational approach [11] in the space where the CART becomes the standard RT. In this algorithm we will consider that $(q,t) \in]0;Q]^2$ with the same sampling Δt and where $Q = \tan(\max\{\omega\})$. Now let $q = t\cos\chi$ (respectively, $q = t\cosh\chi$) in the first (respectively, the second) integral of Equation (24). Thus

$$F_l(t) = \frac{1}{\pi}\int_0^{\frac{\pi}{2}} \mathrm{d}\chi G_l'(t\cos\chi)\sin(l\chi) - \frac{1}{\pi}\int_0^{\cosh^{-1}(Q/t)} \mathrm{d}\chi G_l'(t\cosh\chi) e^{-l\chi}. \tag{25}$$

Now we can define the discretized forms of $F_l(t)$ and $G_l(q)$ as

$$G_{lk} = G_l(k\Delta t) \quad \text{and} \quad F_{lj} = F_l(j\Delta t),$$

where $(j,k) \in [0,K]^2$ with $K = \frac{Q}{\Delta t}$. The derivative $G_l'(q)$ can be approximated by coefficients a_{lk} where

$$a_{lk} = \frac{G_{l(k+1)} - G_{lk}}{\Delta t}.$$

Equation (25) becomes

$$F_{lj} = \frac{1}{\pi}\left[\sum_{k=0}^{j-1} a_{lk}(I_l(\chi j(k+1)) - I_l(\chi jk)) + \sum_{k=j}^{K-1} a_{lk}(J_l(\chi j(k+1)) - J_l(\chi jk))\right],$$

in terms of the primitive

$$I_l(\chi_{jk}) = \int^{\chi_{jk}} \sin(|l|x)\mathrm{d}x = -\frac{\cos(|l|\chi_{jk})}{|l|} \quad \text{for } l \neq 0$$

and

$$J_l(\chi_{jk}) = \int^{\chi_{jk}} e^{-|l|x}\mathrm{d}x = \begin{cases} -e^{-|l|\chi_{jk}}/|l| & \text{if } l \neq 0 \\ \chi_{jk} & \text{if } l = 0, \end{cases}$$

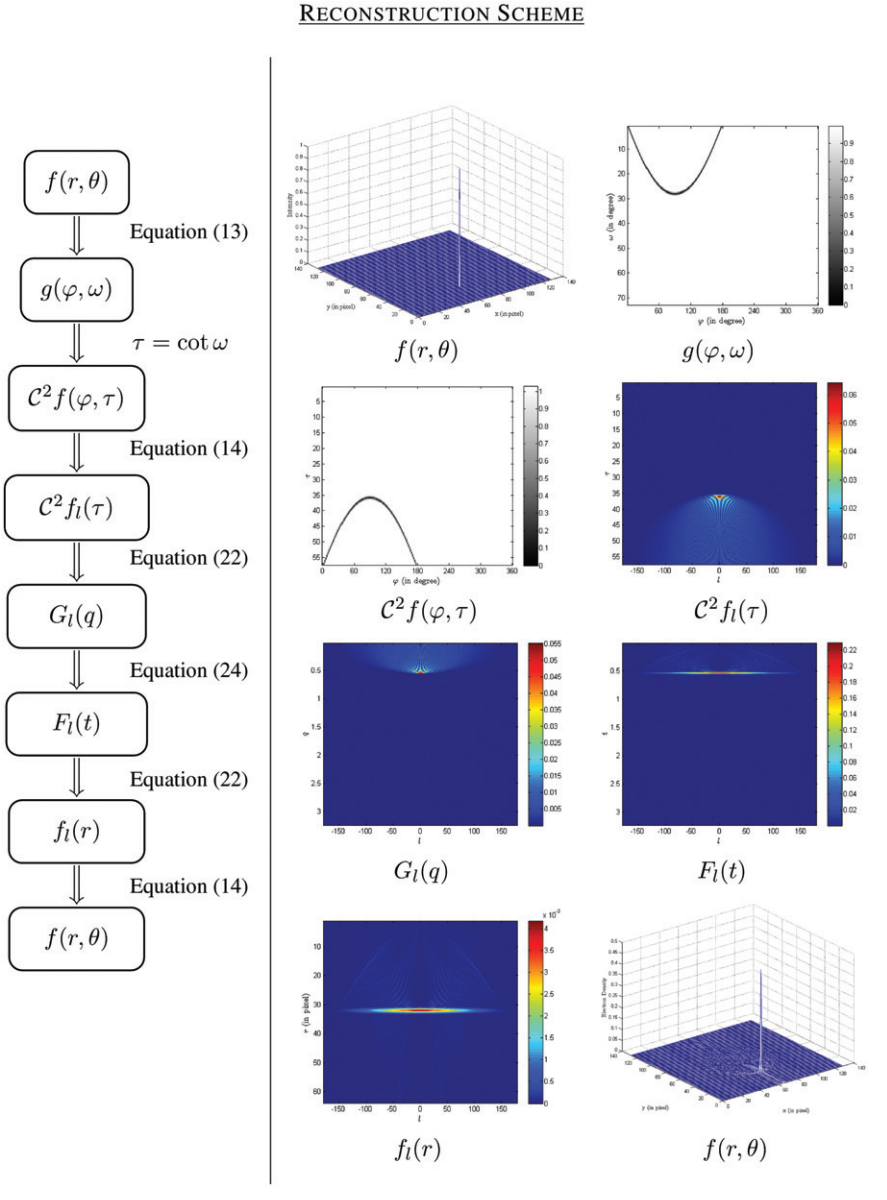

Figure 13. Inversion procedure of the CART_2 and its illustration for the reconstruction of a point object.

where

$$\chi_{jk} = \begin{cases} \cos^{-1}\left(\dfrac{k}{j}\right) & \text{for } 0 \le k \le j \\ \cosh^{-1}\left(\dfrac{k}{j}\right) & \text{for } j \le k \le K. \end{cases}$$

Finally, the discretized form of the reconstruction equation appears as

$$F_{lj} = \frac{1}{|l|\pi}\left[\sum_{k=0}^{j-1} a_{lk}\left(\cos|l|\chi_{j(k+1)} - \cos|l|\chi_{jk}\right) + \sum_{k=j}^{K-1} a_{lk}\left(e^{-|l|\chi_{j(k+1)}} - e^{-|l|\chi_{jk}}\right)\right]. \quad (26)$$

And for $l=0$ a separate expression exists

$$F_{0j} = -\frac{1}{\pi}\sum_{k=j}^{K-1} a_{0k}\left(\chi_{j(k+1)} - \chi_{jk}\right).$$

So having obtained all the F_{lj}, which are the discretized circular components of the associated RT, we recover the theoretical circular components of our circular-arc problem $f_l(r)$ using formula (22) given by

$$f_l(r) = \frac{2p(p^2+r^2)}{(p^2-r^2)^2} F_l\left(\frac{2pr}{p^2-r^2}\right).$$

The final step consists in working out the summation in discrete form:

$$f(r,\theta) = \sum_l f_l(r)e^{il\theta}.$$

We have established an alternative algorithm of image reconstruction based on circular harmonic decomposition for the inverse $CART_2$. This is the image reconstruction method for the new CST modality (CST_2).

5.3. *Simulation results: image reconstructions by $CART_2 - CHD$ and $RT - FBP$*

In this section, we present the numerical simulations of the CART ($CART_2 - CHD$) and compare them with the reconstruction in conventional tomography modelled by the ordinary RT and calculated by the FBP algorithm ($RT - FBP$). Let us recall the classical RT which is defined as integral of an object function on straight lines. The forward RT is:

$$g(u,\varphi) = \int_{\mathbb{R}^2} \mathrm{d}x\,\mathrm{d}y f(x,y)\delta(u - x\cos\varphi - y\sin\varphi),$$

and its inverse transform is

$$f(x,y) = \int_0^{\pi} \mathrm{d}\varphi \int_{-\infty}^{+\infty} \mathrm{d}u \int_{-\infty}^{+\infty} \mathrm{d}\nu|\nu| \times e^{-2i\pi\nu(u - x\cos\varphi - y\sin\varphi)} g(u,\varphi). \quad (27)$$

Equation (27) is called the FBP method. In this case, FBP is an exact inversion formula obtained by combining the action of the ramp filter ($|\nu|$) and the backprojection operation of the RT. This is the most popular inversion method for the ordinary RT owing to its rapid algorithmic implementation.

As an illustration of the feasibility of our new algorithm, we present numerical simulations applied on the medical phantom (Figure 14) and on a cracked concrete image (Figure 15). The scattering medium is discretized with $N \times N$ of length units (pixels). $N = 512$ in the case of the phantom and 256 in the other case. We consider the number of rotational positions N_φ and the number of energy levels N_ω. These numbers define the corresponding angular sampling steps $\mathrm{d}\varphi$ and $\mathrm{d}\omega$ as

$$\mathrm{d}\varphi = \frac{2\,\pi}{N_\varphi} \quad \text{and} \quad \mathrm{d}\omega = \frac{\pi}{2N_\omega}.$$

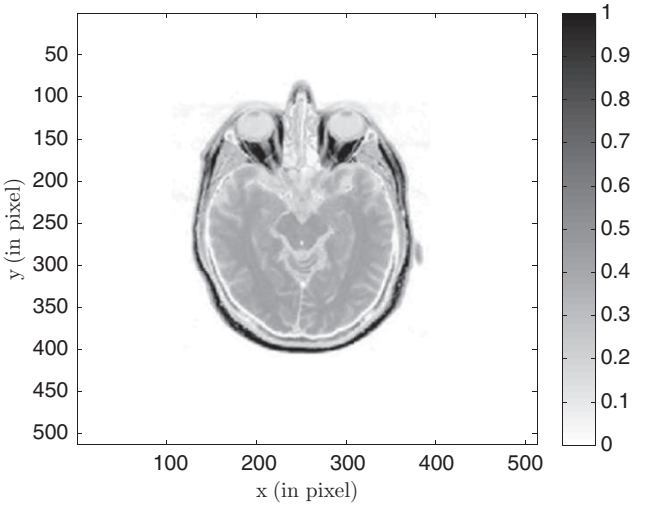

Figure 14. Original of a medical phantom.

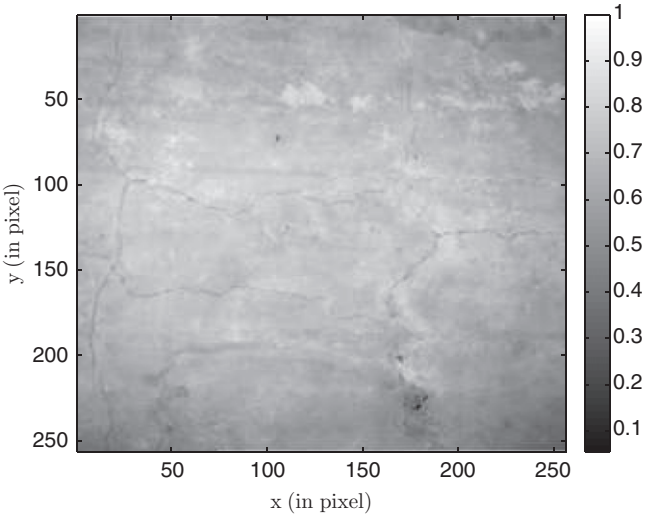

Figure 15. Original of the cracked concrete.

In order to have a 'well-conditioned' problem, the number of projections ($N_\varphi \times N_\omega$) must be larger than or equal to the number of image pixels (N^2). This is why we take $N_\varphi = N_\omega = N$. Moreover, let $p = N$ and $\min\{\omega\} = \mathrm{d}\omega$.

Figures 16 and 17 show the forward Radon transform and CART2 of the Shepp-Logan phantom; Figures 18 and 19 (respectively) show this with respect to the cracked concrete. The $CART_2 - CHD$ approach gives in general a reasonable image quality in the reconstruction of the medical phantom (Figure 20) and of the cracked concrete

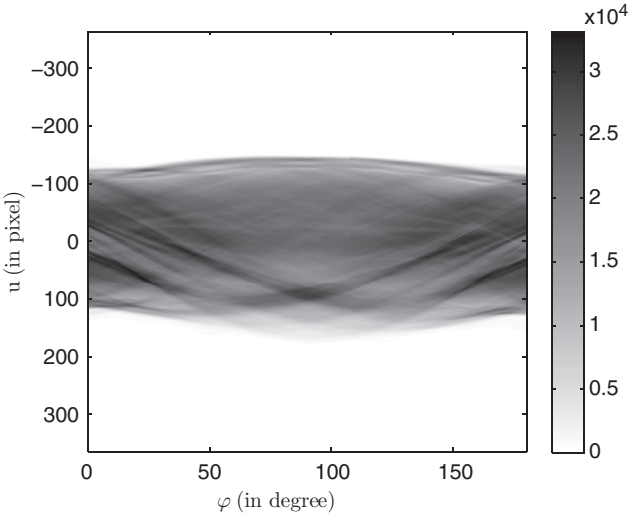

Figure 16. RT of the medical phantom shown in Figure 14.

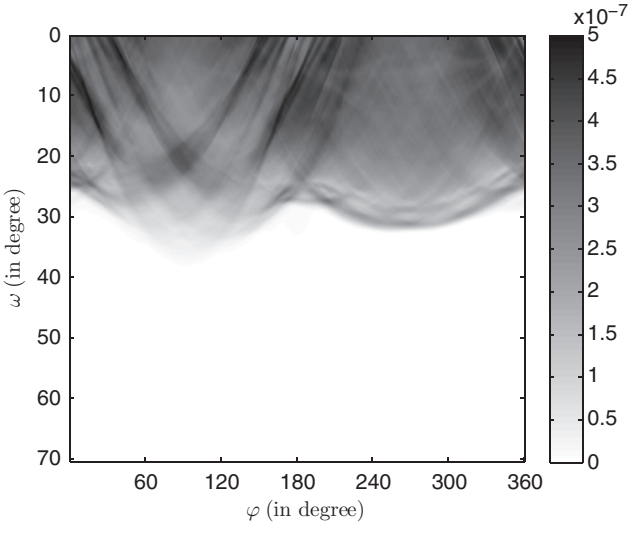

Figure 17. CART_2 of the medical phantom shown in Figure 14.

(Figure 21). Indeed, contours and small structures are well recovered. The numerical error measurements obtained using the $CART_2 - CHD$ are very close to those of the ordinary RT (Figure 22) and are even better in the case of the medical phantom (Figure 23). Nevertheless in the case of the cracked concrete (Figure 21), artefacts are observed in the corners of the medium. This is due to the fact that the studied object occupies the whole medium, the boundary parts are not well scanned and so there is less information concerning these parts. Moreover, the CART_2 works with radial parameters, an object of

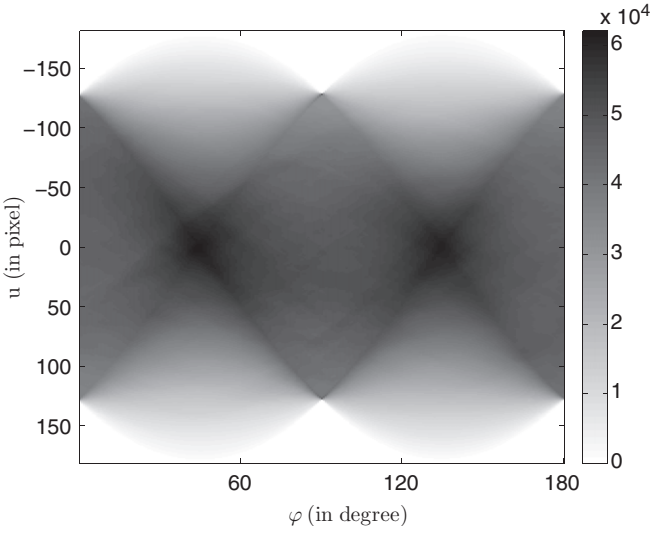

Figure 18. RT of the cracked concrete shown in Figure 15.

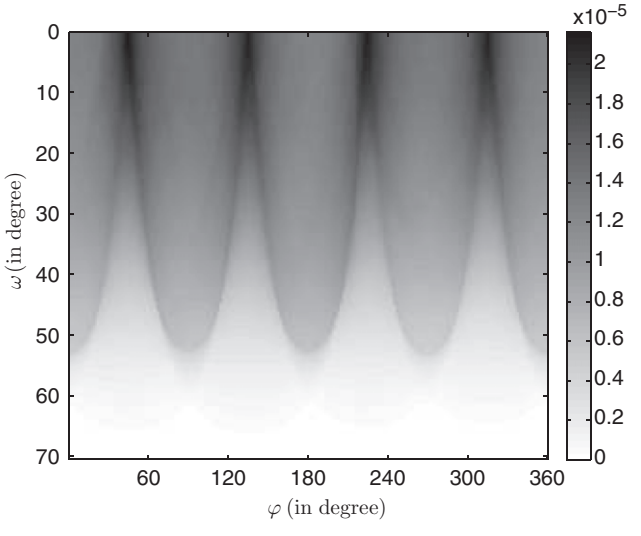

Figure 19. $CART_2$ of the cracked concrete shown in Figure 15.

circular geometry is better suited for this approach. This is the case of the medical phantom.

In spite of this, the interest of our algorithm in the field of medical imaging and of non-destructive testing is incontestable. In order to exhibit the essence of the new CST modality which consists in the use of the scattered radiation as an imaging agent, other factors (such as medium attenuation and Poisson noise) are not taken into account until now. But the influence of these factors will be studied below.

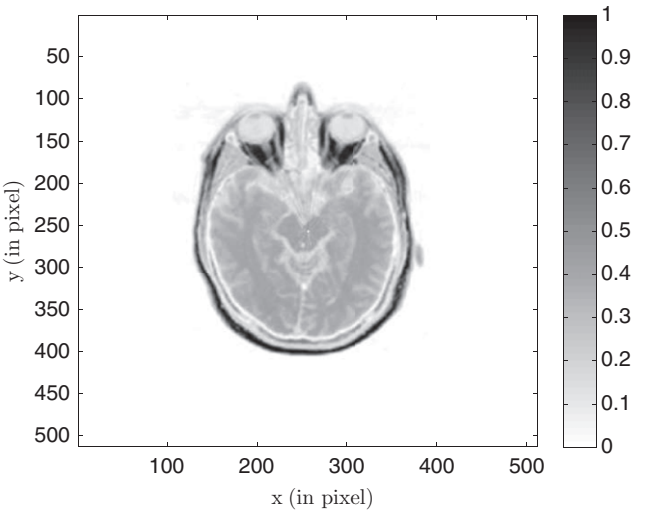

Figure 20. Reconstruction of the medical phantom shown in Figure 14 using $CART_2 - CHD$ and data in Figure 17 with NMAE = 0.49% and NMSE = 0.01%.

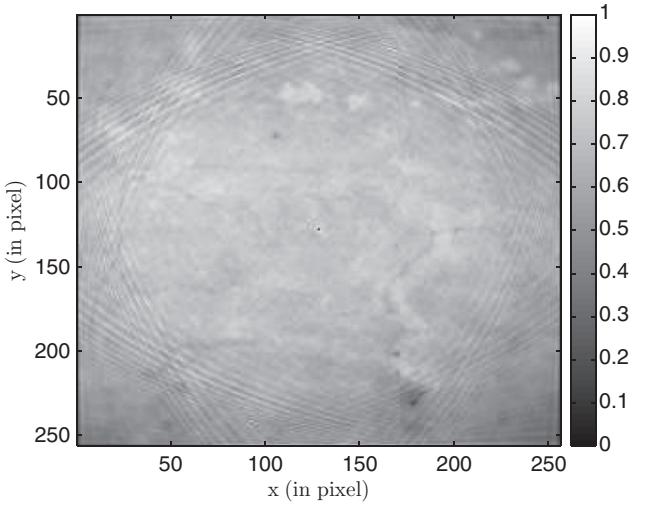

Figure 21. Reconstruction of the cracked concrete shown in Figure 15 using $CART_2 - CHD$ and data in Figure 19 with NMAE = 2.83% and NMSE = 0.3%.

6. Taking into account the physical phenomena in both CARTs

Under realistic working conditions, radiation is affected by medium attenuation and by dispersion due to photometric propagation effects. Moreover, photon emission process follows Poisson's law which generates a hindering noise for data. In this section we study the effects of these phenomena for both CARTs and we now define the following notations,

- dl is the elementary distance on the segment **SM** (or **MD**),

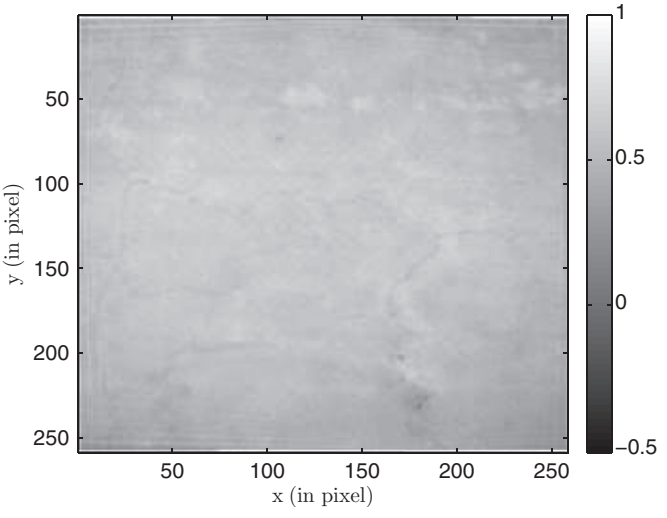

Figure 22. Reconstruction of the cracked concrete shown in Figure 15 using $RT-FBP$ and data in Figure 18 with NMAE = 2.56% and NMSE = 0.2%.

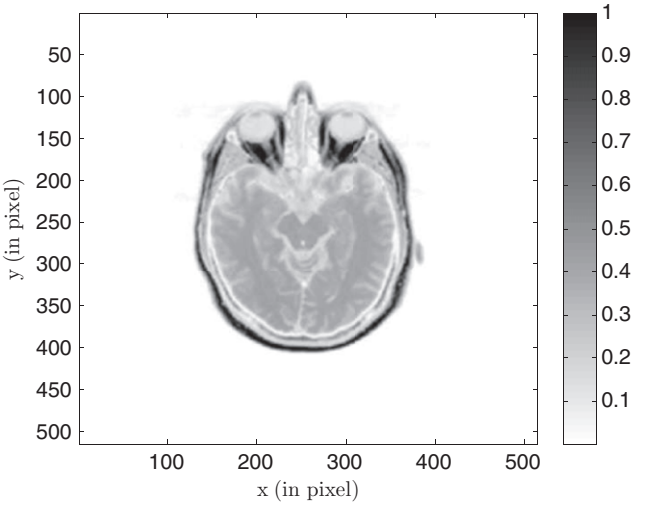

Figure 23. Reconstruction of the medical phantom shown in Figure 14 using $RT-FBP$ and data in Figure 16 with NMAE = 0.59% and NMSE = 0.01%.

- $\overline{\mathbf{SM}}$ stands for the Euclidean distance of the segment **SM**,
- μ_0 (resp. μ_ω) is the linear attenuation map at the energy of the primary radiation (resp. at the energy of the scattered radiation see Equation (1),
- **S**, **M** and **D** are the emitting, scattering and detection points.

6.1. *Influence of the attenuation in CART$_1$: $\mathcal{C}^1_\phi$*

The photometric propagation effects and the Klein–Nishina differential cross section were already taken into account in the Norton's model, thus we have just to add the attenuation factor, W_{att}. In this case $\mathcal{C}^1$ takes the following form $\mathcal{C}^1_\phi$

$$\mathcal{C}^1_\phi f(\rho,\varphi) = \int_0^\pi \mathrm{d}\theta \int_0^\infty \mathrm{d}r\; n_e(r,\theta)\frac{ars(\theta)P(\omega)}{4\pi(2\rho)^3\sin^2\theta}\cdot W_{\text{att}}(r,\theta;\rho,\varphi)\delta[r-2\rho\cos(\theta-\varphi)], \quad (28)$$

where $n_e(r,\theta)$ is the electron density and

$$W_{\text{att}}(r,\theta;\rho,\varphi) = \exp\left(-\int_{(x,y)\in\mathbf{SM}}\mu_0(x,y)\mathrm{d}l\right)\cdot\exp\left(-\int_{(x,y)\in\mathbf{MD}}\mu_\omega(x,y)\mathrm{d}l\right). \quad (29)$$

The term W_{att} cannot be separated in a product $w_1(r,\theta)\cdot w_2(\rho,\varphi)$ and so $\mathcal{C}^1_\phi$ cannot be inverted using the same approach. This is why, we have to propose an attenuation correction algorithm in order to compensate for the attenuation factor.

6.2. *Influence of the physical effects in CART$_2$: $\mathcal{C}^2_\phi$*

Taking into account the attenuation and the dispersion of radiation

$$\frac{e^{-\int_{\mathbf{SM}}\mu_0(x,y)\mathrm{d}l}}{\overline{\mathbf{SM}}^2}\frac{e^{-\int_{\mathbf{MD}}\mu_\omega(x,y)\mathrm{d}l}}{\overline{\mathbf{MD}}^2} \quad \text{with} \quad \overline{\mathbf{SM}}^2\overline{\mathbf{MD}}^2 = (p^2-r^2)^2(1+\tau^{-2}),$$

and the Klein–Nishina probability $P(\omega)$, the CART$_2$ ($\mathcal{C}^2$) takes the following form $\mathcal{C}^2_\phi$:

$$\mathcal{C}^2_\phi n_e(\varphi,\tau) = \frac{P\left(\tan^{-1}\left(\frac{1}{\tau}\right)\right)}{(1+\tau^{-2})}\int_{-\frac{\pi}{2}}^{\frac{\pi}{2}} W'_{\text{att}}(\varphi,\tau,\gamma)\frac{r(\gamma)n_e(r(\gamma),\gamma+\varphi)}{(p^2-r(\gamma)^2)^2}\;\frac{\sqrt{1+\tau^2}}{\sqrt{1+\tau^2\;\cos^2\gamma}}\mathrm{d}\gamma, \quad (30)$$

where

$$W'_{\text{att}}(\varphi,\tau,\gamma) = \exp\left(-\int_{(x,y)\in\mathbf{SM}}\mu_0(x,y)\mathrm{d}l\right)\cdot\exp\left(-\int_{(x,y)\in\mathbf{MD}}\mu_\omega(x,y)\mathrm{d}l\right).$$

The inversion of Equation (30) is not known at present, therefore an attenuation correction has to be applied.

6.3. *Correction of the attenuation factor: iterative pre correction algorithm*

Attenuation is a very important issue especially for CST. Numerous methods exist to correct this factor. Among these methods the Iterative Pre Correction algorithm (IPC) [13] proposes to correct the data before reconstruction as follows.

To simplify notation, we put $\mathbf{t}=(\rho,\varphi)$ (resp. $\mathbf{t}=(\varphi,\tau)$) for the CART$_1$ (resp. CART$_2$) and we call $\mathcal{T}$ the corresponding measurement space. Then we write the operator of the corrected physical CART as

$$\tilde{\mathcal{C}_\phi}\colon n_e(r,\theta)\longrightarrow\frac{\mathcal{C}_\phi n_e(\mathbf{t})}{A(\mathbf{t})},$$

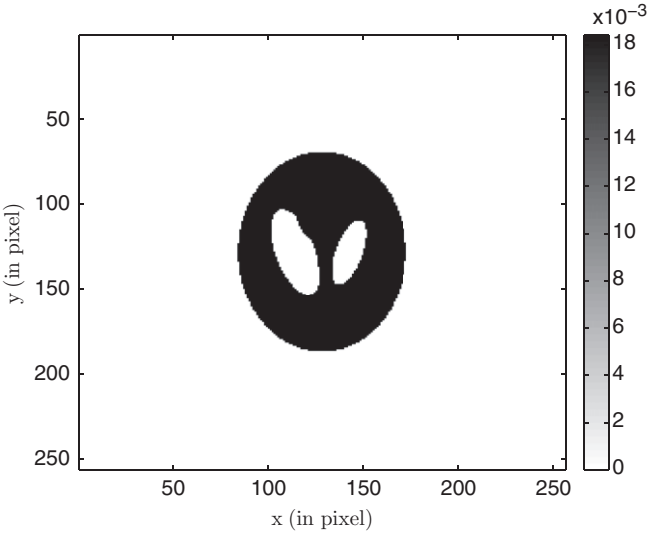

Figure 24. Attenuation map of the medium with a size (30 cm × 30 cm harr; 256 × 256 pixels).

with $A(\mathbf{t})$ the correction function and $\mathcal{C}_\phi$ is either $\mathcal{C}_\phi^1$ or $\mathcal{C}_\phi^2$. Therefore the IPC algorithm is expressed by the following recurrence relation on $(n_e)_n$, which is the nth-order correction of n_e

$$(n_e)_{n+1} = (n_e)_n + \mathcal{C}^{-1}\tilde{\mathcal{C}}_\phi\big(n_e - (n_e)_n\big) \quad \text{with } (n_e)_0 = 0.$$

Of course, we do not know n_e but $\mathcal{C}_\phi n_e$. Considering that the number of circulars arcs for both CART is limited and indexed by the integer pair (k, l), then the correction function corresponds to the following correction matrix:

$$A_{kl} = \frac{1}{N_i}\sum_{i=1}^{N_i} \exp\left(\frac{\overline{\mathbf{S}^{kl}\mathbf{M}_i^{kl}}}{N_j}\sum_{j=1}^{N_j}\mu_0(x_{ij}^{kl}, y_{ij}^{kl}) - \frac{\overline{\mathbf{M}_i^{kl}\mathbf{D}^{kl}}}{N_j}\sum_{j=1}^{N_j}\mu_\omega(x_{ij}^{kl}, y_{ij}^{kl})\right),$$

with N_i the number of calculated points, $\mathbf{M}_i^{kl}$ for each circular arc $C(k, l)$, N_j the number of calculated points for each segments ($\mathbf{S}^{kl}\mathbf{M}_i^{kl}$ and $\mathbf{M}_i^{kl}\mathbf{D}^{kl}$) and $(x_{ij}^{kl}, y_{ij}^{kl})$ the cartesian coordinates of the corresponding segments.

In order to illustrate the attenuation correction, we have chosen the attenuation of the water (0.157 cm^{-1}) and the shape of the attenuating medium as presented in Figure 24, the original electron density (3.34×10^{23} cm^{-3}) and its shape in Figure 25. Figures 26 and 27 show the electron density reconstructed by $CART_1 - CHD$ and $CART_2 - CHD$ but without attenuation correction. We notice that the degradation of the magnitude due to the attenuation factor is more important in the CART_1 case than in the CART_2 case (4×10^{19} against 2.5×10^{19}). But the shape of the degradation is more homogenous in the CART_1 case than in the CART_2 case. Figures 28 and 29 show the same reconstructed electron densities with the attenuation correction by the IPC algorithm after 20 steps for CART_1 and 10 steps for CART_2. The magnitude (around 5×10^{20}) is well-recovered and quality of the reconstructed images proves the efficiency of the correction.

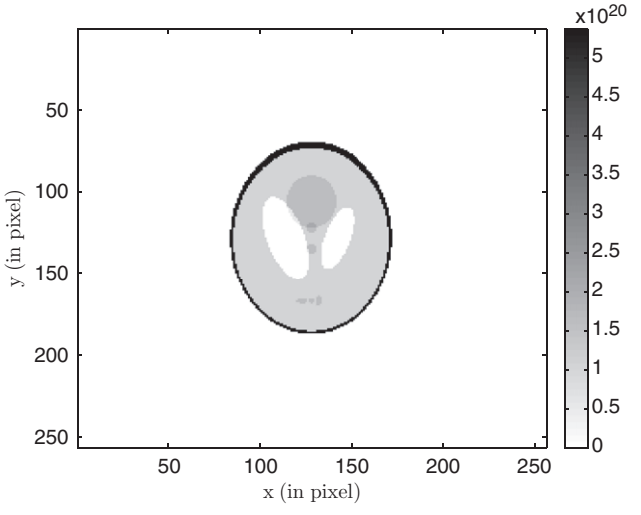

Figure 25. Original electron density on an attenuating medium represented in Figure 24.

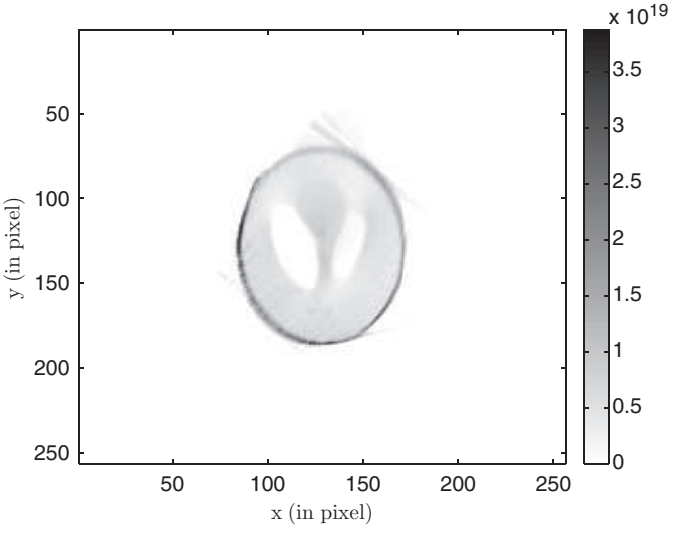

Figure 26. Reconstruction of the electron density Figure 25 without correction using $CART_1 - CHD$.

6.4. *Poisson noise robustness*

Since photon emission process follows Poisson's law, this phenomenon is one of the main cause of degradation of the quality of image reconstruction in CST (Here we study the robustness of our algorithms by taking into account this phenomenom, but we do not look for a way to denoise it). Thus, the projections become in both cases $\tilde{g}(\mathbf{t}) \sim \mathcal{P}(\mathcal{C}f(\mathbf{t}))$ where $\mathcal{P}$ stands for the Poisson's law. In order to evaluate the robustness of our algorithms,

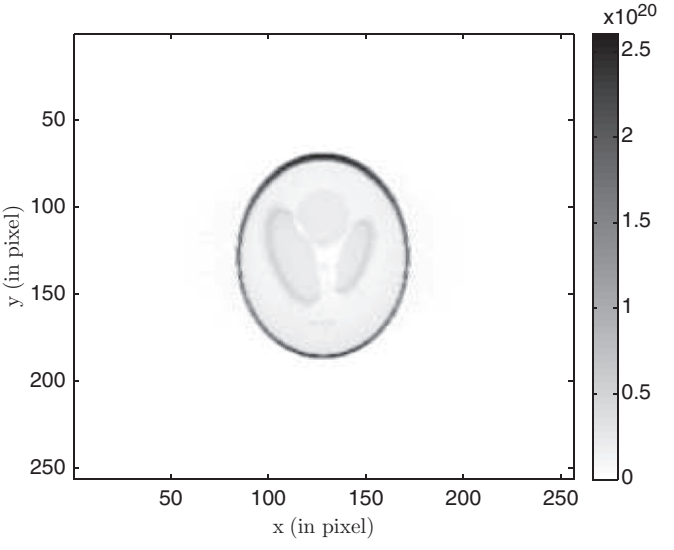

Figure 27. Reconstruction of the electron density Figure 25 without correction using $CART_2 - CHD$.

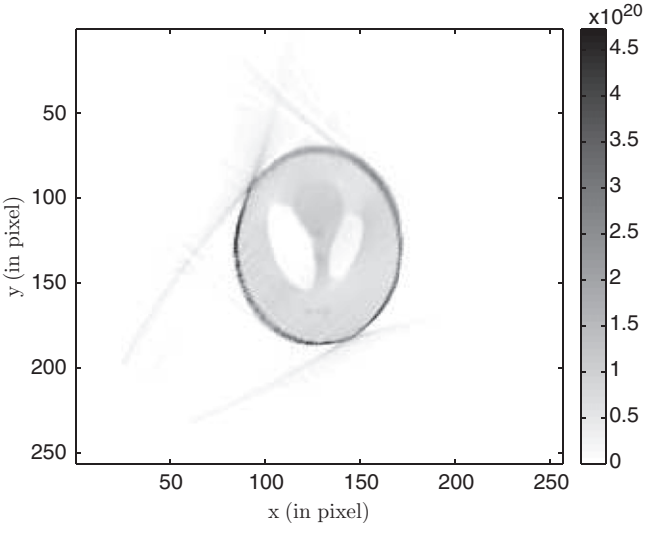

Figure 28. Reconstruction of the electron density Figure 25 using $CART_1 - CHD$ and IPC algorithm.

we use the following signal-to-noise ratio (SNR):

$$SNR = 10\log\left(\int_{\mathbf{t}\in\mathcal{T}} \mathcal{C}f(\mathbf{t})^2 \mathrm{d}\mathbf{t}\right) - 10\log\left(\int_{\mathbf{t}\in\mathcal{T}} |\tilde{g}(\mathbf{t}) - \mathcal{C}f(\mathbf{t})|^2 \mathrm{d}\mathbf{t}\right).$$

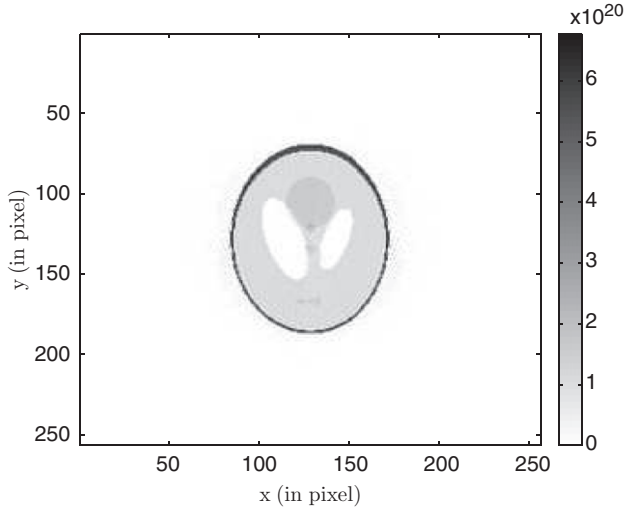

Figure 29. Reconstruction of the electron density Figure 25 using $CART_2 - CHD$ and IPC algorithm.

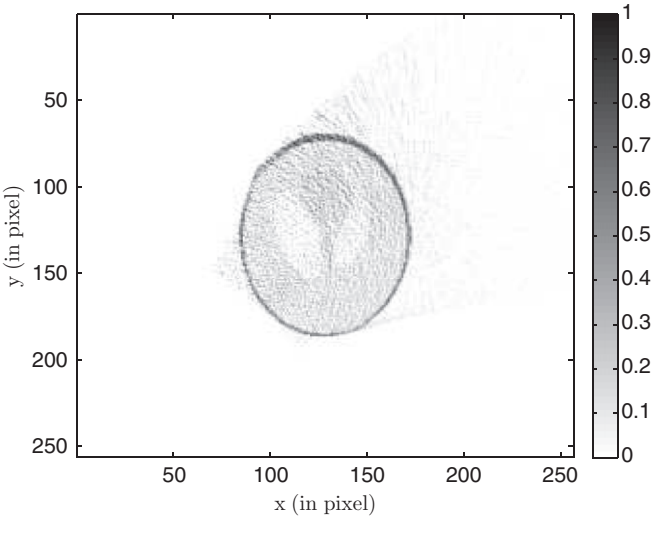

Figure 30. Reconstruction of the Shepp–Logan phantom using $CART_1 - CHD$ with SNR = 10 dB.

We carried out the reconstruction of the Shepp–Logan phantom by CART_1 and CART_2 at two different SNR. When $SNR = 10$ dB, the phantom is not well recovered (Figures 30 and 31). With $SNR = 25$ dB the phantom and its small structures are well observed (Figures 32 and 33). Hence, it is interesting to apply a denoising method (like curvelets [14]) before the reconstruction.

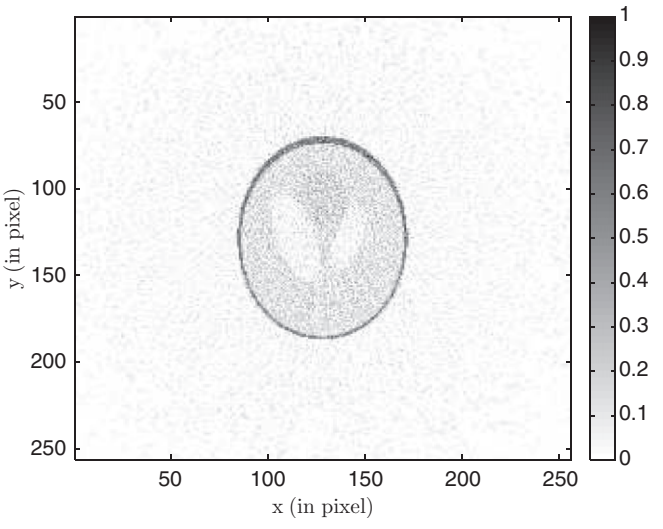

Figure 31. Reconstruction of the Shepp–Logan phantom using $CART_2 - CHD$ with SNR = 10 dB.

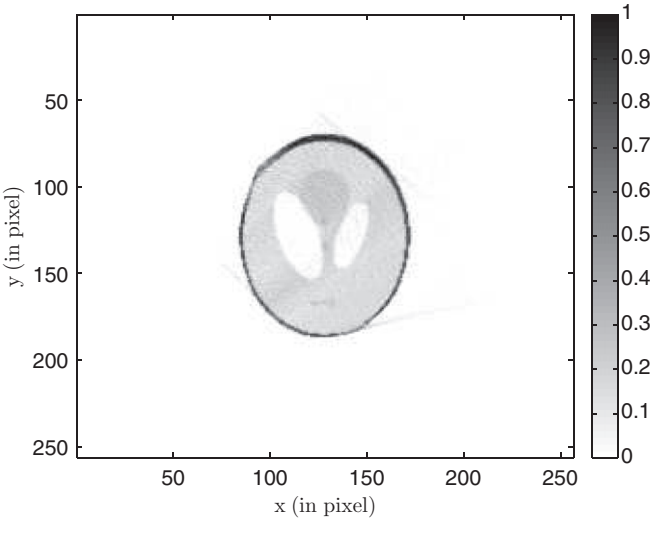

Figure 32. Reconstruction of the Shepp–Logan phantom using $CART_1 - CHD$ with SNR = 25 dB.

7. Conclusion and perspectives

We have established two algorithms for the numerical inversion of two CARTs defined on two remarkable classes of circles in the plane. These two CART arise from the modelling of two CST modalities. Based on the circular harmonic decomposition, the advantage of these algorithms is to produce a reconstructed image which is consistent with the data (forward transforms) as opposed to analytical conventional methods such as the 'FBP'

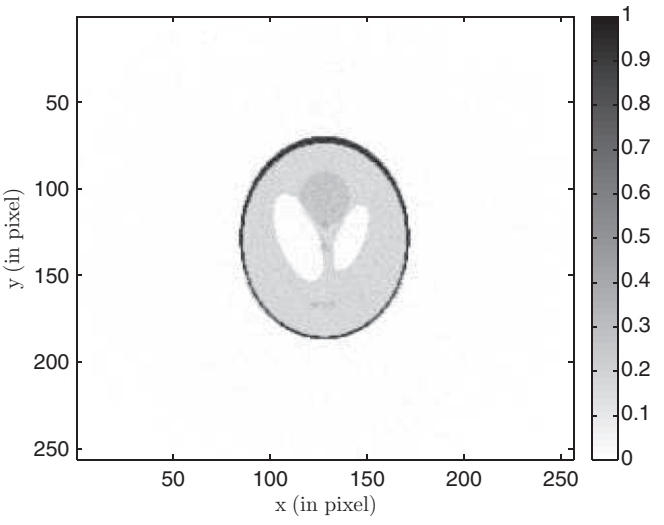

Figure 33. Reconstruction of the Shepp–Logan phantom using $CART_2 - CHD$ with SNR = 25 dB.

algorithm, without further computational complexity. Moreover, the use of iterative algorithms like IPC in order to correct the attenuation factor gives good results for both transforms and the result of robustness to the Poisson noise is presented (a good reconstruction without denoising is observed for a SNR equal to 25 dB).

The simulation results show the feasibility of the CST which is suited for biomedical imaging or non-destructive testing and could represent an alternative to X-ray tomography. Norton's CST seems to be suited for scanning large objects and for nondestructive testing where both the radiation source and the detector are placed on the same side of the object and without rotation, whereas ours gives more details on small structures and boundaries.

In CST, matter is characterized by its electron density (scattering sites) which is an alternative to its attenuation map provided by X-ray radiology. Moreover, in this imaging the problems caused by Compton effect (such as blurs, loss of contrast of image, false detections whose resolution remains a major technical challenge until now in conventional tomography) is nicely solved by the CARTs.

The CST and CART open the way to some future promising works : extension of bi-dimensional CST to three-dimensional transmission Compton scattering imaging for example, or combining the transmission and emission Compton imaging to form a new bimodal imaging based on scattered radiation.

References

[1] H. Zaidi and K.F. Koral, *Scatter modelling and compensation in emission tomography*, Eur. J. Nucl. Med. Mol. Imag. 31 (2004), pp. 761–782.

[2] P.G. Lale, *The examination of internal tissues, using gamma-ray scatter with a possible extension to megavoltage radiography*, Phys. Med. Biol. 4 (1959), pp. 159–167.

[3] R.L. Clarke, E.N.C. Milne, and G.V. Dyk, *The use of Compton scattered gamma rays for Tomography*, Inv. Radiol. 11 (1976), pp. 225–235.

[4] G. Harding, H. Strecker, and R. Tischler, *X-ray imaging with Compton-scatter radiation*, Philips Tech. Rev. 41 (1983), pp. 46–59.
[5] N.V. Arendtsz and E.M.A. Hussein, *Energy-spectral Compton scatter Imaging – Part 1: Theory and mathematics*, IEEE Trans. Nucl. Sci. 42 (1995), pp. 2155–2165.
[6] S.J. Norton, *Compton scattering tomography*, J. Appl. Phys. 76 (1994), pp. 2007–2015.
[7] M.K. Nguyen and T.T. Truong, *Inversion of a new circular-arc Radon transform for Compton tomography*, Inv. Probl. 26 (2010), p. 065005.
[8] J. Radon, *Uber die bestimmung von funktionnen durch ihre integralwerte langs gewisser mannigfaltikeiten*, Ber. Verh. Sachs. Akad. Wiss. Leipzig-Math. Natur. Kl. 69 (1917), pp. 262–277.
[9] A.M. Cormack, *The Radon transform on a family of curves in the plane*, Proc. Am. Math. Soc. 83 (1981), pp. 325–330.
[10] A.M. Cormack, *Radon's problem – Old and new*, SIAM-AMS Proc. 14 (1984), pp. 33–39.
[11] C.H. Chapman and P.W. Cary, *The circular harmonic Radon transform*, Inv. Probl. 2 (1986), pp. 23–49.
[12] A.K. Louis, *Orthogonal function series expansions and the null space of the Radon transform*, SIAM J. Math. Anal. 15 (1984), pp. 621–633.
[13] A. Maze, J.L. Cloirec, R. Collorec, Y. Bizais, P. Briandet, and P. Bourguet, *Iterative reconstruction methods for nonuniform attenuation distribution in SPECT*, J. Nucl. Med. 34 (1993), pp. 1204–1209.
[14] B. Zhang, M.J. Fadili, and J.L. Starck, *Wavelets, ridgelets and curvelets for poisson noise removal*, IEEE Trans. Image Process. 17 (2008), pp. 1093–1108.